IUST
Iran University of Science and Technology

Iranian Journal of Electrical and Electronic Engineering

Journal Homepage: ijeee.iust.ac.ir

An Impedance-Matched Exponentially-non-Uniform Axial-Mode Helical Antenna

A. Abimbola Ayorinde*, S. Adeniyi Adekola* and I. Mowete*(C.A.)

Abstract: This paper, using the circuit-geometric features of the Method of Moments (MoM), presents a comprehensive analytical treatment of an exponentially non-uniform helical antenna (ENH), mounted on a ground plane of finite extent. Earlier investigations reported in the literature established that the introduction of an exponential non-uniformity in the turns spacing of an otherwise uniformly wound helical antenna significantly improves its axial ratio and power gain profiles, but failed to address two important questions; one concerning the influence of the degree of non-uniformity on the antenna performance: and the other, the associated return loss profile, which is of particular importance in practical applications. It is shown in this paper, that when a properly designed impedance matching circuitry is introduced, a return loss of the ENH of close to 60 dB is achievable; without compromising axial ratio and gain performances. Indeed, axial ratio bandwidth remained unchanged at 54.55% for both the impedance-matched and unmatched ENHs, whilst maximum gain changed marginally from 14.19dB, for the unmatched ENH to 14.18dB for the impedance-matched antenna.

Keywords: Axial Mode, Exponential non-Uniformity, Helical Antenna, Impedance Matching, Return Loss.

1 Introduction

IMPEDANCE matching, for the helical antenna operating in the axial mode preferred in many applications, has, over the years, been the subject of quite a few research investigations, [1] – [4]. Stegen [1], in one of the earliest reported contributions, suggested that the axial mode helical antenna's input impedance is critically dependent on the method utilized for connecting the antenna to the terminating transmission line; and then empirically demonstrated the effectiveness of a two-section impedance transformer for impedance matching purposes. A few years later, [2], after noting that the inherent nominal input impedance for the class of uniformly wound axial-mode helical antennas is close to 140Ω, described a simpler method involving a single wire, with which the input impedance can be tuned to the more desirable value of 50Ω. A variation of this approach was reported by [3], whose peripherally fed antenna included a wire conductor of specified dimensions, incorporated into the antenna's first turn, as a matching section. The 'self-impedance matching' technique introduced in [4] for the hemispherical, center-fed helical antenna also utilizes a copper strip attached to the feed line, as the matching mechanism. In a more recent contribution, [5] reported the use, of an impedance transformer, of a copper strip bonded to a center-fed compact (2-turn, 2-pitch) helical antenna, between the tip of the antenna conductor and the feed point. An excellent summary of the design details, merits, and disadvantages of these approaches is available in [6], whose choice of the models due to [2] and [3] for adaptation, enabled the design and implementation of a single wire impedance matching network for a uniformly wound axial-mode helical antenna. The authors of [6], in a follow-up publication [7], reported experimental and simulation results, which indicated that the influence of the matching network on the antenna's radiation pattern is insignificant. This conclusion is supported by the results presented in [8],

Iranian Journal of Electrical & Electronic Engineering, 2023.
Paper first received 08 Jan 2023 and accepted 13 Sep 2023.
* The author is with the Department of Electrical & Electronics Engineering, University of Lagos, Akoka, Lagos Nigeria.
E-mails: aayorinde@unilag.edu.ng, adekola_sulaiman@yahoo.com, amowete@unilag.edu.ng.
Corresponding Author: I. Mowete.

for an axial-mode helical antenna, impedance matched through the use of a single short wire.

According to [9], the relative ease with which uniformly wound axial mode helical antennas (or normal mode, non-uniformly wound helical antennas [10]) are matched to 50Ω feed lines does not extend to non-uniformly wound cases, mainly because as observed elsewhere [4], the antenna's turns become very closely spaced, at one end of its non-uniform distribution. Because the introduction of non-uniformity into the geometry of axial mode helical antennas has been demonstrated, [9], [11] – [14], to significantly improve gain and circular polarization performance profiles, impedance matching for the antennas represents an important practical application issue that has yet to receive research attention. It is consequently the main objective of this paper, to investigate the performance of an impedance-matched, non-uniformly wound, axial mode helical antenna, using the exponentially non-uniform geometry as a candidate. First, the paper examines the influence of the degree of non-uniformity (as defined by an 'exponential variation factor', which prescribes the proximity of the antenna's turns at the feed end) on the input and far-zone performance parameters. Thereafter, and using a modification of the 'matching network' described in [2], [6] and [7], the effects of impedance matching on the performance parameters are comprehensively examined.

Computational results available from a moment-method formulation and solution of the problem suggest some interesting properties for the impedance-matched exponentially non-uniform axial mode helix. One of the conclusions arising from the results is that the antenna's axial ratio and gain profiles depend significantly on the degree of geometrical non-uniformity introduced by the exponential variation of the turn spacing. The results also indicate that the single wire 'matching network' utilized in the paper massively improves the antenna's return loss performance with minimal effects on the gain and axial ratio profiles.

The paper, in section 2, presents the moment-method-based analytical foundations of the model utilized, and in section 3, presents and discusses the computational results obtained for the model. A summary of the key findings and associated conclusions are presented in section 4, which is the paper's concluding section.

2 Analysis

Figure 1 displays the problem geometry for an N-turn thin-wire helical antenna of a circular cross-section, whose turn spacing varies exponentially along the z-axis. The exponentially non-uniform helical antenna (ENH) is mounted above a finite circular ground plane modeled by wire grids of thin-wire conductors.

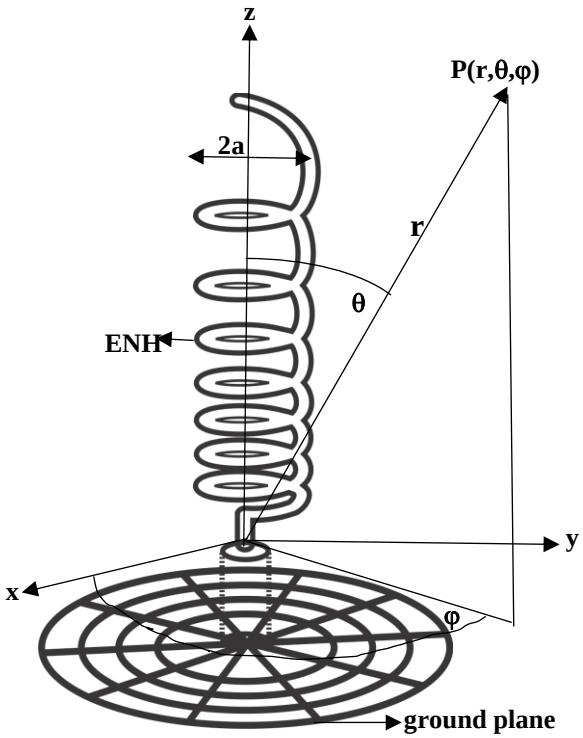

Fig. 1 Problem geometry of an exponentially-non-uniform helix above a circular ground plane of finite extent.

This geometry may be described analytically in terms of a position vector denoted by $\bar{r}'$ directed from the origin of the coordinate system to any point on the antenna according to [9]

$$\bar{r}' = a\cos\phi'\hat{u}_x + a\sin\phi'\hat{u}_y + p(e^{\kappa\phi'} - 1)\hat{u}_z \quad (1)$$

where a stands for the helix radius, ϕ' is the running angular variable along the ENH geometry and ranges from 0 to $2\pi N$, and the two constants (p, κ) together define the degree of exponential non-uniformity of the turns-spacing and are specified in this paper through a restriction of equal axial lengths of the ENH and an equivalent uniformly wound helical antenna. For the latter, variation along the z-axis is given by:

$$z' = (a\tan\alpha)\phi' \quad (2)$$

in which α represents the antenna's constant pitch angle. For the ENH, the pitch angle denoted by α_e is inherently dependent on ϕ' in the following manner:

$$\alpha_e = \tan^{-1}\left(\frac{dz'}{ad\phi'}\right) = \tan^{-1}\left(\frac{p\kappa e^{\kappa\phi'}}{a}\right) \quad (3)$$

as given by a differentiation of the z-component of Eq. (1) concerning ϕ'. By imposing the restriction of equal axial extent on the ENH and its corresponding uniformly wound helical antenna, the constant p is obtained as

$$p=\frac{2\pi Natan\alpha}{\left(e^{2\pi N\kappa}-1\right)} \tag{4}$$

a substitution of Eq. (4) in Eq. (1) leads to the following expression for the ENH geometry;

$$\bar{r}^{'}=acos\phi'\hat{u}_x+asin\phi'\hat{u}_y+\frac{2\pi Natan\alpha}{\left(e^{2\pi N\kappa}-1\right)}\left(e^{\kappa\phi'}-1\right)\hat{u}_z \tag{5}$$

so that κ, here referred to as the exponential variation factor, becomes the only variable that defines the antenna's degree of non-uniformity. It is a matter of interest to note that through an application of the L′ Hospital rule, the position vector expression of Eq. (5) reduces to that of a uniformly wound helical antenna when κ assumes a value of zero. The unit vector denoted by $\hat{u}_{\ell'}$ along the ENH wire is given by:

$$\hat{u}_{\ell}=\frac{d\bar{r}'}{d\phi'}\Big/\left|\frac{d\bar{r}'}{d\phi'}\right|=\frac{-\sin\phi'\hat{u}_x+cos\phi'\,\hat{u}_y+\left(p\kappa e^{\kappa\phi'}/a\right)\hat{u}_z}{\sqrt{1+\left(p\kappa/a\right)^2e^{2\kappa\phi'}}} \tag{6}$$

whereas the differential arm length of the ENH denoted by $d\ell'$ derives from the fact that:

$$d\ell'=\sqrt{\left(dx'\right)^2+\left(dy'\right)^2+\left(dz'\right)^2}$$

which, for the ENH geometry. ultimately reduces to

$$dl'=a\sqrt{1+(p\kappa/a)^2e^{2\kappa\phi'}}\,d\phi' \tag{7}$$

The total arm length of the ENH can then be obtained by integrating Eq. (7) from 0 to 2πN according to

$$L=a\int_0^{2\pi N}\sqrt{1+(p\kappa/a)^2e^{2\kappa\phi'}}\;d\phi' \tag{8}$$

where N represents the number of helical turns. And it is readily verified that the integration resolves into

$$L=\frac{1}{\kappa}\left[\begin{array}{l}\sqrt{a^2+(p\kappa)^2e^{4\pi N\kappa}}-\frac{a}{2}ln\left(1+\frac{2a}{\sqrt{a^2+(p\kappa)^2e^{4\pi N\kappa}}-a}\right)\\ -\frac{1}{\kappa}\sqrt{a^2+(p\kappa)^2}\,]-\frac{a}{2}ln\left(1+\frac{2a}{\sqrt{a^2+(p\kappa)^2}-a}\right)\end{array}\right] \tag{9}$$

With these results, the vector magnetic potential, conventionally denoted by $\bar{A}$ admits expression as

$$\bar{A}=\frac{\mu_o}{4\pi}\int_0^L\hat{u}_{\ell'}I(\ell')[\frac{e^{-j\beta_o\left|\bar{r}-\bar{r}'\right|}}{\left|\bar{r}-\bar{r}'\right|}]\,d\ell' \tag{10}$$

provided that $\bar{r}$ is the position vector from the origin of the coordinate system to the far-field point P(r, θ, φ), $\bar{r}'$ position vector for a point on the thin-wire antenna geometry, (β_o, μ_o) free-space propagation constant and free-space permeability, respectively, $I(\ell')$ filamentary current distributed along the antenna axis, $d\ell'$ differential length of the antenna and $\hat{u}_{\ell'}$ unit vector along the wire antenna. When the conventional far-field 'magnitude and phase approximations' are invoked according to

$$|\bar{r}-\bar{r}'|=r \tag{11a}$$

and

$$\left|\bar{r}-\bar{r}'\right|=r-\hat{u}_r\bullet\bar{r}' \tag{11b}$$

respectively, and noting that

$$\hat{u}_r=sin\theta\cos\varphi\hat{u}_x+sin\theta sin\varphi\hat{u}_y+\cos\theta\hat{u}_z \tag{11c}$$

then the use of Eq. (1) for $\bar{r}'$ in Eq. (11b), yields:

$$\left|\bar{r}-\bar{r}'\right|=r-\hat{u}_r\bullet\bar{r}'=r-asin\theta cos\left(\varphi-\phi'\right)-pcos\theta\left(e^{\kappa\phi'}-1\right) \tag{11d}$$

substitution of Eq. (6), (7), (11a) and (11d) in Eq. (10) leads to:

$$\bar{A}=\frac{\mu_o ae^{-j\beta_o r}}{4\pi r}\int_0^{2\pi N}\left[-sin\phi'\hat{u}_x+cos\phi'\hat{u}_y+\left\{\frac{p\kappa e^{\kappa\phi'}}{a}\right\}\hat{u}_z\right]\times\left[I\left(\phi'\right)e^{j\beta_0\left[asin\theta\cos(\varphi-\phi')+pcos\theta\left(e^{\kappa\phi'}-1\right)\right]}\right]d\phi' \tag{12}$$

whose Cartesian components are then readily determined as:

$$A_x=\frac{\mu_o ae^{-j_o r}}{4\pi r}\int_0^{2\pi N}-sin\phi'I\left(\phi'\right)e^{j\beta_o\left[asin\theta\cos\left(\varphi-\phi'\right)+pcos\theta\left(e^{\kappa\phi'}-1\right)\right]}\,d\phi' \tag{13a}$$

$$A_y=\frac{\mu_o ae^{-j_o r}}{4\pi r}\int_0^{2\pi N}cos\varphi'I\left(\phi'\right)e^{j\beta_o\left[asin\theta\cos\left(\varphi-\varphi'\right)+pcos\theta\left(e^{\kappa\varphi'}-1\right)\right]}\,d\phi' \tag{13b}$$

and

$$A_z=\frac{\mu_o ae^{-j_{\beta o}r}}{4\pi r}\int_0^{2\pi N}\left[\frac{p\kappa}{a}\right]e^{\kappa\varphi'}I\left(\phi'\right)e^{j\beta_o\left[asin\theta\cos\left(\varphi-\phi'\right)+pcos\theta\left(e^{\kappa\phi'}-1\right)\right]}\,d\phi' \tag{13c}$$

using the well-known rectangular-spherical coordinates transformation expressions

$$A_{\vartheta}=\cos\theta\cos\varphi A_x+\cos\theta\sin\varphi A_y-\sin\theta A_z \tag{14a}$$

$$A_{\varphi}=-\sin\varphi A_x+\cos\varphi A_y \tag{14b}$$

therefore, the corresponding spherical components of the vector potential $\bar{A}$ emerge as:

$$A_{\theta}=\frac{\mu_o ae^{-j\beta_o r}}{4\pi r}\int_0^{2\pi N}\left[cos\theta\sin\left(\varphi-\phi'\right)-sin\theta\left(\frac{\kappa p}{a}\right)e^{\kappa\phi'}\right]\times\left[I\left(\phi'\right)e^{j\beta_o\left[asin\theta\cos\left(\varphi-\phi'\right)+pcos\theta\left(e^{\kappa\phi'}-1\right)\right]}\right]d\phi' \tag{15a}$$

$$A_{\varphi}=\frac{\mu_o ae^{-j\beta_o r}}{4\pi r}\int_0^{2\pi N}\left[\cos\left(\varphi-\phi'\right)\right]I\left(\phi'\right)e^{j\beta_o\left[asin\theta\cos\left(\varphi-\phi'\right)+pcos\theta\left(e^{\kappa\phi'}-1\right)\right]}\,d\phi' \tag{15b}$$

in the far zone of the antenna, the electric field is simply related to the vector potential according to

$E_{\vartheta}=-j\omega A_{\theta}$ and $E_{\varphi}=-j\omega A_{\varphi}$: hence

$$E_{\theta}=\frac{-j\omega\mu_o ae^{-j\beta_o r}}{4\pi r}\int_0^{2\pi N}\left[cos\theta\sin\left(\varphi-\phi'\right)-sin\theta\left(\frac{\kappa p}{a}\right)e^{\kappa\phi'}\right]\times\left[I\left(\phi'\right)e^{j\beta_o\left[asin\theta\cos\left(\varphi-\phi'\right)+pcos\theta\left(e^{\kappa\phi'}-1\right)\right]}\right]d\phi' \tag{16a}$$

$$E_{\varphi}=\frac{-j\omega\mu_o a e^{-j\beta_o r}}{4\pi r}\int_0^{2\pi N}\left[\cos(\varphi-\phi')\right]I(\phi')e^{j\beta_o\left[a\sin\theta\cos(\varphi-\phi')+p\cos\theta\left(e^{\kappa\phi'}-1\right)\right]}\,d\phi' \tag{16b}$$

It is easily ascertained that when the constant p is set to zero and N to unity in Eq. (16a) and (16b), these field expressions reduce to:

$$E_{\theta}=\frac{-j\omega\mu_o a e^{-j\beta_o r}}{4\pi r}\int_0^{2\pi}\left[\cos\theta\sin(\varphi-\phi')\right]I(\phi')e^{j\beta_o a\sin\theta\cos(\varphi-\phi')}\,d\phi' \tag{17a}$$

$$E_{\varphi}=\frac{-j\omega\mu_o a e^{-j\beta_o r}}{4\pi r}\int_0^{2\pi}\left[\cos(\varphi-\phi')\right]I(\phi')e^{j\beta_o a\sin\theta\cos(\varphi-\phi')}\,d\phi' \tag{17b}$$

which together, represent radiation field expressions for a circular-loop antenna located on the z = 0 plane, and are exactly the same as those reported elsewhere, [15]: to serve as a preliminary check on the correctness of the analytical results. To complete the analysis, an account is required for the circular ground plane of finite extent, associated with the ENH structure. As suggested by Fig. 1, the ground plane is modeled by a wire grid comprising some circular loops and radial elements. These elements contribute to the radiation field as 'scatterers' excited by the ENH. In the case of each circular loop, the scattered fields are given by Eq. (17a) and (17b) as

$$E_{\theta}=\frac{-j\omega\mu_o a_k e^{-j\beta_o r}}{4\pi r}\int_0^{2\pi}\left[\cos\theta\sin(\varphi-\phi')\right]I(\phi')e^{j\beta_o a_k\sin\theta\cos(\varphi-\phi')}\,d\phi' \tag{18a}$$

$$E_{\varphi}=\frac{-j\omega\mu_o a_k e^{-j\beta_o r}}{4\pi r}\int_0^{2\pi}\left[\cos(\varphi-\varphi')\right]I(\phi')e^{j\beta_o a_k\sin\theta\cos(\varphi-\varphi')}\,d\phi' \tag{18b}$$

where a_k represents the radius of the k[th] circular loop element and a_K = b for the outermost circular element. On the other hand, corresponding field expressions for the radial elements are exemplified by [16]:

$$E_{\theta}=\frac{-j\omega\mu_o e^{-j\beta_o r}\cos\theta\cos\left(\varphi-\phi'_m\right)}{4\pi r}\int_0^{b}I(\ell')e^{j\beta_o\ell'\sin\theta\cos\left(\varphi-\phi'_m\right)}\,d\ell' \tag{19a}$$

$$E_{\varphi}=\frac{-j\omega\mu_o e^{-j\beta_o r}\sin\left(\varphi-\phi'_m\right)}{4\pi r}\int_0^{b}I(\ell')e^{j\beta_o\ell'\sin\theta\cos\left(\varphi-\phi'_m\right)}\,d\ell' \tag{19b}$$

provided that φ'_m, which denotes the angle subtended by the m[th] radial element and the x-axis, is given by

$$\phi'_m=\frac{2\pi}{M}(m-1),\quad m=1,2,\ldots,\mathrm{M} \tag{19c}$$

and M represents the number of radial elements. The size of the finite ground plane, relative to the radius of the ENH is here specified by an "aspect ratio" symbolized by γ and defined according to:

$$\gamma=\frac{b}{a} \tag{20}$$

If it is then supposed that the wire-grid model consists of K circular loop elements and M radial elements, the resultant far-field components are obtained by the superposition of contributions from the various component elements as follows:

$$E_{\theta}=E_{\theta}^{e}+\sum_{k=1}^{K}E_{\theta}^{ck}+\sum_{m=1}^{M}E_{\theta}^{lm} \tag{21a}$$

$$E_{\varphi}=E_{\varphi}^{e}+\sum_{k=1}^{K}E_{\varphi}^{ck}+\sum_{m=1}^{M}E_{\varphi}^{lm} \tag{21b}$$

in which the superscripts *e*, *c*, and *l* identify the ENH, circular loop, and radial elements, respectively.

Finally, and for impedance matching, a version of the 'single, thin-wire' model utilized by Savić et al [6, 7] is adopted as pictorially described in Fig. 2.

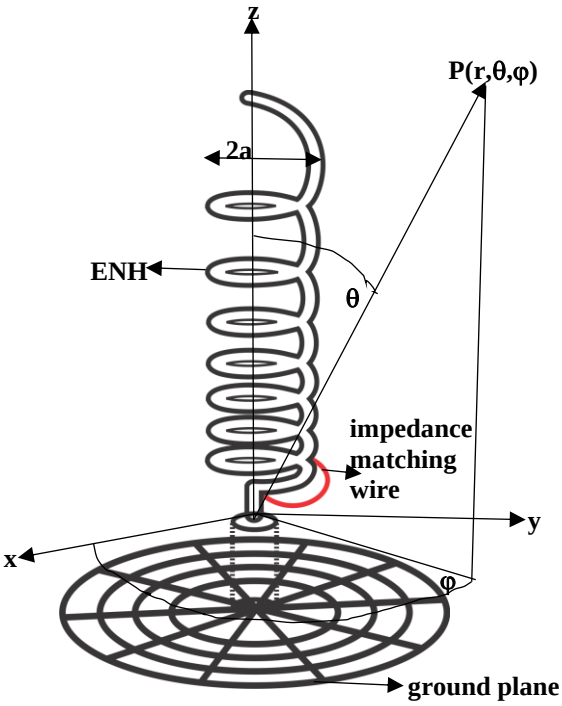

Fig. 2 The exponentially non-uniform helical antenna including a thin-wire impedance matching network.

In this case, the impedance-matching thin wire extends from the tip of the ENH helix and terminates on the helix at the end of one-quarter of the first turn. Thus, the coordinates of the first point on the impedance-matching arc are x = a, y = 0, and z = 0, while those of the last point are given by x = 0, y = a, and $z=p\left(e^{\kappa\pi/2}-1\right)$. The locus of the geometry of the matching wire, in between these extremes, is fully described by the following equations:

$$x = g\cos\psi$$
$$y = g\sin\psi \tag{22}$$
$$z = 2p\left(e^{\kappa\psi} - 1\right)$$

where

$$\psi = \frac{(t-1)\pi/2}{a}, \qquad t = 2,3, \ldots, 8 \tag{22a}$$

with

$$g = a\left(\frac{1.02}{C_\lambda} + 0.3691\right) \quad \kappa = 0.01, \tag{22b}$$

and

$$g = a\left(\frac{1.05}{C_\lambda} + 0.3691\right), \quad 0.02 \le \kappa \le 0.06 \tag{22c}$$

In these expressions, a stands for the ENH radius and C_λ ENH's circumference, expressed in units of wavelengths.

As will be seen in due course, the main effect of the matching network is to occasion a redistribution of current along the axis of the ENH such that the antenna is effectively matched to a 50 Ω transmission line without any discernible effect on the antenna's far-zone parameters.

Current distributions along the ENH wire axis as well as the induced currents along circular loops and radial elements axes, which essentially represent the only unknown quantities in the foregoing analytical exposition, can then be completely determined with the use of the method of moments, in a manner described elsewhere [14], [17].

With the current distributions available, all antenna parameters of interest can be determined through expressions given in the ensuing discussions, for completeness' sake.

2.1 Input Impedance and Return Loss

Feed-point input impedance symbolized by Z_{in} for the ENH is given by

$$Z_{in} = \frac{V_{in}}{I_{in}} = R_{in} + jX_{in} \tag{23}$$

where R_{in} is the resistive part and X_{in} the reactive part, V_{in} excitation voltage at the feed-point, and I_{in} current at the feed-point of the ENH. Given the antenna's input impedance, the return loss can be determined from, [18],

$$Return\,Loss\,(dB) = 20log_{10}\left|\frac{Z_{in}+Z_T}{Z_{in}-Z_T}\right| \quad (dB \tag{24}$$

where in this paper $Z_T = Z_o$, the characteristic impedance of the coaxial cable feeding the antenna, taken as $50\,\Omega$.
It is very important to remark that the expression for return loss utilized here has been identified by an erstwhile Editor-in-Chief of the IEEE Transactions on Antennas and Propagation, [18], as the correct expression, contrary to the impression given by a more widely used expression.

2.1 Axial Ratio and Power Gain

The axial ratio (AR) of the radiated fields which is a measure of the degree of circular polarization of the fields is determined [19], as:

$$AR(dB) = 10log_{10}\left[\frac{|E_\varphi|^2 \sin^2\chi + |E_\theta|^2 \cos^2\chi + |E_\varphi||E_\theta|\cos\delta\sin 2\chi}{|E_\varphi|^2 \cos^2\chi + |E_\theta|^2 \sin^2\chi - |E_\varphi||E_\theta|\cos\delta\sin 2\chi}\right] \tag{25}$$

provided that

$$\chi = \frac{1}{2}tan^{-1}\left[\frac{2|E_\varphi||E_\theta|\cos\delta}{|E_\theta|^2 - |E_\varphi|^2}\right] \tag{25a}$$

and that δ represents the phase difference between field components E_θ *and* E_φ. On the other hand, the power gain G_p(dB) which defines the antenna efficiency is evaluated from, [20]:

$$G_p\,(dB) = 10log_{10}\left[\frac{|E_\theta|^2 + |E_\varphi|^2}{30|I_{in}|^2 R_{in}}\right] \tag{26}$$

where R_{in} and I_{in} are as defined in Eq. (23).

Numerical results obtained from the computer implementation of the foregoing analytical results are the subjects of discussion in section three, which follows.

3 Computational Results and Discussion

In addition to the preliminary validation of the analytical results as provided by associated discussions in section 2, further validation is offered through comparisons of computational results due to these expressions with corresponding simulation and measurement data for an unmatched ENH, reported in [9]. Figure 3 displays comparative results for axial ratio, the main focus of the performance evaluation of the 4-turn, 'exponentially spaced helical antenna (ESH), whose parameters are provided in [9].

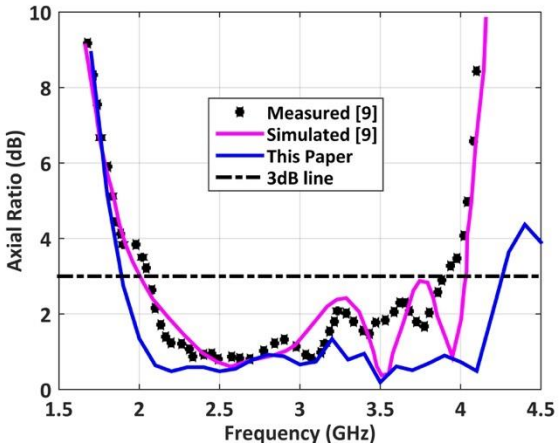

Fig. 3 Comparison of ENU Axial Ratio performance due to this paper's formulation with corresponding simulation and measurement results of Fig.2 of [9].

Simulation and measurement data were obtained from Fig. 2 of [9] through the use of the commercial software 'GetData Graph Digitizer'. The good agreement between the axial ratio profiles of Fig. 3 as well as the axial ratio bandwidth of 65.6% (compared with 67% of [9]) due to this paper's formulation supports the validity of the formulation.

Other computational results presented in this section derive from an antenna's physical structure defined by the following parameters.

Aspect ratio (γ): 5

Exponential variation factor (κ):

$0 \leq \kappa \leq 0.06$

ENH circumference in wavelengths (C_λ):

$0.80 \leq C_\lambda \leq 1.40$

Number of ENH turns (N): 7

Number of circular loops in the wire-grid plane (K): 6

Number of radial elements in the wire-grid plane (M): 6

ENH height above the ground plane 0.15λ

Feeding co-axial cable characteristic impedance Z_o: 50Ω

Pitch angle of the corresponding uniform helix (α): 12.5^o

Centre frequency: 2.0GHz.

3.1 Current Distributions

Representative cases of profiles of the distribution of current along the axis of the ENH for given frequencies (or C_λ) and different values of exponential variation factor (κ) are graphically presented in Fig. 4. It is easily seen from Fig. 4.a that the magnitude of the feed-point current increases as the exponential variation factor increases, most likely due to increase in proximity of the first few turns of ENH as κ increases. In addition, it is seen from Fig. 4.a that when κ is less than 0.04, the current profiles are basically characterized by two regions, namely, an exponentially decaying region from the feed-point to about the first 2½ turns of the antenna, and a surface wave profile over the remaining turns of the ENH. As a consequence of marked flaring out at the open end of ENH, the extent of current reflection is minimal as evidenced by the minor standing wave profile at that end. On the other hand, for $\kappa = 0.06$, for which the ENH turns in the neighborhood of the feed end are extremely close to each other occasioning strong interactions between the turns, and consequently, relatively higher values of feed-point current as suggested by the much stronger exponentially decaying current wave along the ENH; as well as correspondingly higher reflected current components, as revealed by the significant ripples on the current profile.

When C_λ assumes a value of 1.00 which is generally referred to as the optimum electrical circumference for the uniform helix, [21], current distribution profiles for degrees of exponential non-uniformity are displayed in Fig. 4.b. These profiles share the same general characteristics as those earlier described for the $C_\lambda = 0.80$ cases. However, in this case, the exponential decaying regions are more or less restricted to the first 1½ turns of the ENH. It is a matter of interest to observe that for $C_\lambda = 1.00$ magnitudes of feed-point currents for various values of κ are not too different, with the uniform helix having the largest value. Also, at this frequency, the intensity of current reflection from the open end is not significant for different values of κ. On the other hand, from Fig. 4.c, discernible increments in magnitudes of feed-point currents of ENH are noticeable when $C_\lambda = 1.20$, and in this case, the end of the exponential decaying component has shifted inwards to the first turn of the ENH.

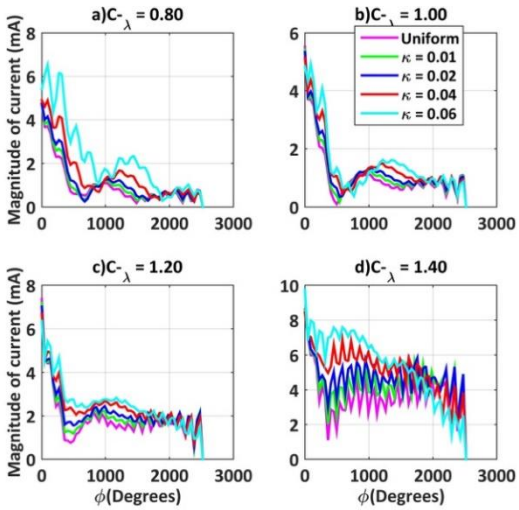

Fig. **4** Profiles of current distribution along the axis of the ENH for different degrees of non-uniformity at given frequencies.

The profiles reveal that the magnitude of feed-point current decreases as κ increases, and because current reflections from the open end have now increased significantly, nearly all the currents on the entire arm's length of the ENH are typified by ripples.

The profiles of Fig. 4.d are for C_λ = 1.40, for different values of κ; and for these degrees of non-uniformity, significant distortions feature in the two current distribution regions identified as characteristic of ENH. Also in this case, the extent of current reflection from the open end is quite substantial as demonstrated by the strong ripples superimposed on all the current plots, and this may be attributed to a large increase in the ENH's arm lengths at C_λ = 1.40. With changes in C_λ and κ, the ENH's arm length changes, and the profiles of Fig. 5. describe how these changes influence the distribution of the magnitude of current, for different degrees of exponential non-uniformity. The case of κ equals zero, which corresponds to a uniformly wound helix is depicted in Fig. 5.a, and clearly shows, as may be expected [22] that the feed-point current magnitude assumes higher values as C_λ increases (as the arm length increases) and most pronounced when C_λ = 1.40.

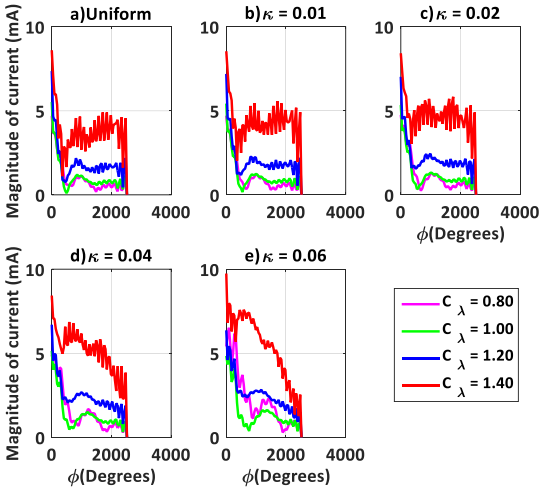

Fig. 5 Profiles of current distribution along the axis of the ENH at different frequencies for given degrees of non-uniformity.

Figure 5.a also highlights the fact that the current reflection from the open end of the helix becomes more pronounced as C_λ increases. Unlike the other curves, the distribution for the C_λ = 1.40 case is almost entirely of the standing wave type. These features of the distribution of the magnitude of current are also displayed for the ENH defined by κ = 0.01, 0.02, and 0.04, though with noticeable differences in the current magnitude as can be seen from Figs. 5.b – 5.d, respectively. Expectedly at κ = 0.01, the influence of exponential non-uniformity is minimal as reflected by the resemblances of the current profiles of the two cases for all values of C_λ. An interesting observation is that for κ = 0.04, the minimum point of the exponentially decaying section of the magnitude of current when C_λ = 0.80 has shifted towards the open end as can be observed from Fig. 5.d. An examination of the profiles for κ = 0.06 (Fig. 5.e) reveals that magnitude of the feed-point current for C_λ = 0.80 (for which arm length is smallest) is significantly greater than those for C_λ = 1.00 and C_λ = 1.20, and slightly less than that for C_λ = 1.40. It is also observed that for most of the span of the arm length of the ENH when C_λ = 1.00 and 1.20, the current plots are of surface wave type with only a small fraction of the span accommodating the exponentially decaying current; on the other hand, profiles of the distributions of the magnitude of current for the cases C_λ = 0.80 and 1.40 are essentially traveling waves with prominently visible ripples, due to high current reflection from the open end.

3.2 Radiation Fields

Using the expressions developed in section 2 and the distribution of current characterized by the magnitude profiles discussed in the foregoing, computational results were obtained for the far-zone fields of the ENH. Representative results described in this section are for the φ = 0° plane and first, for only the normalized theta component (E_θ) patterns, because as will be seen shortly, the E_φ components display virtually identical characteristics. The field pattern profiles of Fig. 6 are for the E_θ fields for values of C_λ between 0.80 and 0.95. When C_λ = 0.80, it can be seen that all the major lobes of the ENH's E_θ patterns for various values of κ considered are symmetrical and well-aligned about the helix axis (θ = 0°) including the special case of uniform helix, with negligible side lobes but moderate back lobes. The back lobe along the θ = 180° for the case κ = 0.06 is the most pronounced, and this may be attributed to the nature of its current distribution discussed earlier. When C_λ is increased to 0.85, the main lobes of the ENH's E_θ patterns still remain in the forward direction, that is, along θ = 0°, with noticeable differences in beam widths and varying degrees of non-uniformity.

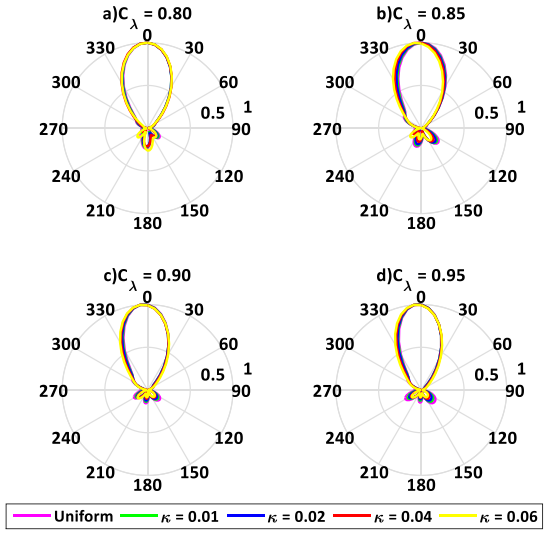

Fig. 6 Theta-components of the radiation E-field patterns in the XZ-plane for varying degrees of non-uniformity with $0.8 \le C_{\lambda} \le 0.95$.

Although the patterns are still characterized by insignificant side lobes, the back lobes are more noticeable in directions other than the θ = 180° axis. For the cases of C_λ = 0.90 and 0.95, an important departure from those characterizing features is that the radiation in the backward direction has reduced considerably though in the case of the latter, the back lobes in the θ = 135° direction are of higher strength.

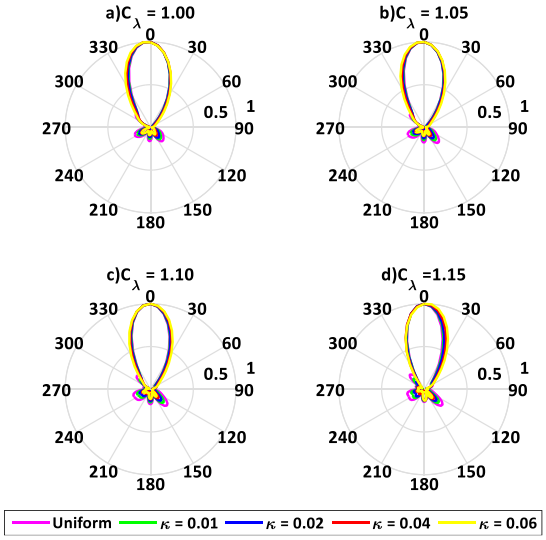

Fig. 7 Theta-components of the radiation E-field patterns in the XZ-plane for varying degrees of non-uniformity with $1.00 \le C_{\lambda} \le 1.40$.

Fig. 7 displays the radiation patterns of E_θ components of the ENH for values of C_λ between 1.00 and 1.15. It is evident from the patterns that the major lobes which, like those of Fig. 6, are directed along the helical axis (θ = 0°) are also well-formed with a high degree of symmetry about the axis, with significantly suppressed sidelobes. Similar comments apply for the E_θ patterns for C_λ = 1.10 and 1.15, though the side lobes, in this case, are of slightly stronger strength in the last quadrant. The back lobes of the E_θ patterns may be described as being of modest strengths, with the exception of patterns for κ = 0.06.

For the sake of completeness, comparisons of representative normalized E_θ and E_φ radiation-zone patterns of the ENH for different values of κ and values (1.15 and 1.25) for C_λ are displayed in Figs. 8 and 9, respectively.

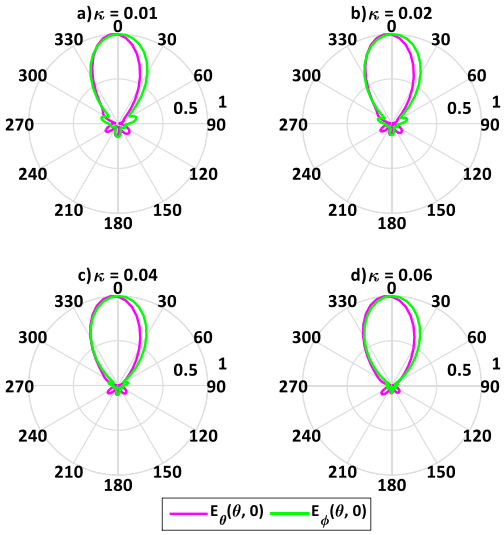

Fig. 8 Comparison of corresponding E_θ and E_φ components of the field radiated by the ENH for C_{λ} = 1.15.

The normalized patterns of Fig. 8 show that for C_λ = 1.15 and κ = 0.01 and 0.02, the main lobes of the E_θ patterns have slightly smaller beam-widths compared with those of the E_φ patterns; in addition, the E_φ patterns are characterized by stronger side lobes while E_θ patterns are typified by higher back-lobes levels, though lobes are within the 'insignificant limits', for both patterns. Although the beam widths of the patterns become almost the same when κ = 0.04 and 0.06, in comparison with the corresponding patterns for κ = 0.01 and 0.02, their side lobes and back lobes are of considerably reduced intensity.

Normalized corresponding E_θ and E_φ patterns for different values of κ, with C_λ = 1.25 are compared in Fig. 9, from which it can be observed that though all the major lobes of the patterns are well-formed, they are not entirely symmetrical about the helical axis (θ = 0°). Also, for this case, the normalized E_θ patterns seem to have lower-sized beam widths than those of the E_φ patterns, for all values of κ considered.

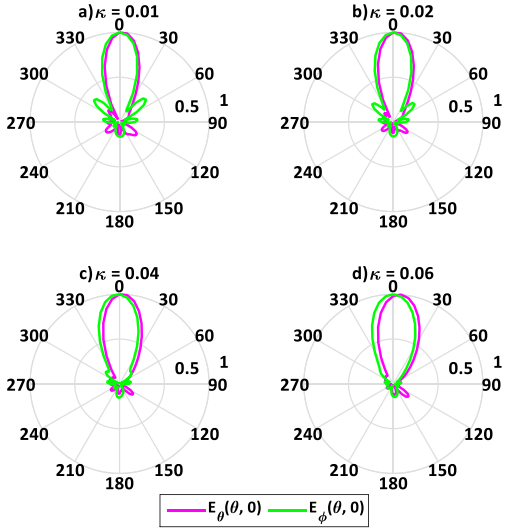

Fig. 9 Comparison of corresponding E_θ and E_φ components of the field radiated by the ENH for $C_\lambda = 1.25$.

For κ = 0.01 and 0.02, the side lobes of the E_φ patterns have higher intensity when compared with those of E_θ patterns, while the back lobes of both patterns are of somewhat equivalent strength. The higher levels of non-uniformity defined by κ = 0.04 and 0.06, lead, in this case, to noticeable asymmetry about θ = 0° in the main lobes of both patterns with the E_φ patterns having moderately higher beam widths in comparison with the E_θ patterns. On the other hand, the side lobes and back lobes of both patterns are of much smaller strengths relative to those of cases κ = 0.01 and 0.02. It may be inferred that as κ increases, some improvements are noticed in the main lobes' beam widths of the E_θ and E_φ patterns at C_λ equals values of 1.15 and 1.25. In addition, as κ assumes higher values, both the side lobes and back lobes of the E_θ and E_φ patterns are characterized by a reduction in intensity.

3.3 Influence of the Matching Network

The influence of the impedance-matching network on the return loss, axial ratio, and power gain of the ENH will be evaluated via the comparative performance of the ENH with and without the matching network.

3.3.1 Return Loss

Fig. 10 displays the return loss (RL) plots of the ENH with and without an impedance-matching circuitry discussed in section 2 of this paper. It is evident from the RL profiles that without the impedance matching wire RL values are less than 10dB as may be expected [18], for almost all values of κ and C_λ. The interesting exceptions to this occur when $C_\lambda = 1.40$ for all values of κ and when $C_\lambda = 0.8$ for κ = 0.06 for which the RL value is close to 17dB. Nonetheless, from a practical viewpoint, the aforementioned values of return loss are inadequate for satisfactory power transfer purposes.

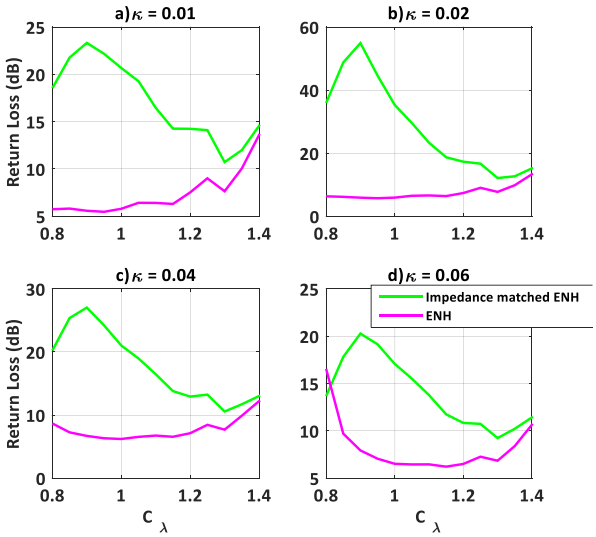

Fig. 10 Return Loss Characteristics of the ENH with and without impedance matching.

When the impedance matching circuitry is introduced, however, the RL values become significantly enhanced as evident from the RL profiles of ENH with impedance-matching wire. All the four RL profiles for the impedance-matched ENH share the interesting features that maximum values are recorded at $C_\lambda = 0.9$, and that the best RL values are obtained when $0.8 \le C_\lambda \le 1.1$. It is also a matter of interest to observe that corresponding RL values for κ = 0.01, 0.04. and 0.06 are comparable, those for κ = 0.02 are generally higher, as a matter of fact, the remarkable RL value of 54.91 dB is recorded when $C_\lambda = 0.9$ at κ = 0.02.

One way of examining the impact of the impedance-matching arrangement on the far-field characteristics of the ENH is to regard the profiles of the antenna's axial ratio and power gain with and without the inclusion of the impedance-matching circuitry.

3.3.2 Axial Ratio and Power Gain

The curves of Fig. 11 compare the axial ratio performances of the ENH when it is impedance-matched and without impedance-matching.

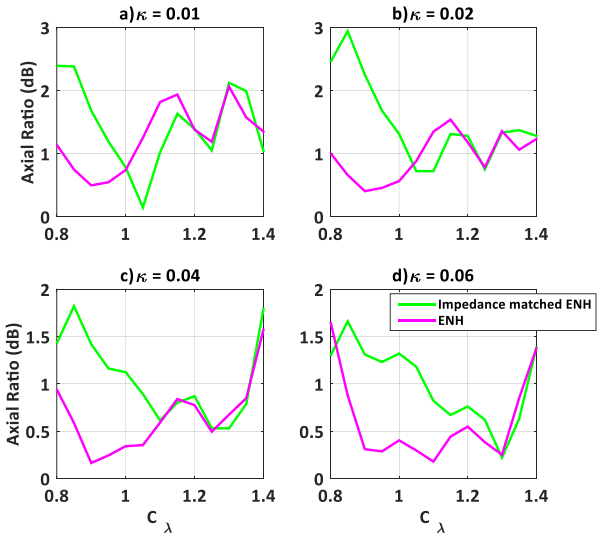

Fig. 11 Profiles of the axial ratio of the ENH with and without impedance matching.

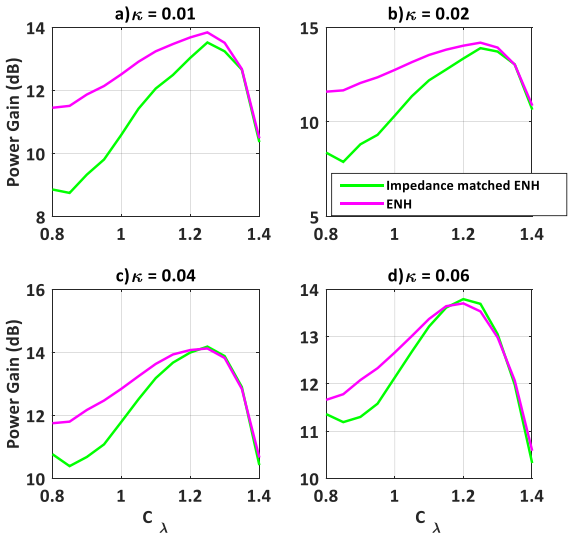

Fig. 12 Effects of impedance matching on the power gain response of the ENH.

The profiles of Fig. 11 reveal some notable features concerning the influence of impedance matching on the axial ratio performance of the ENH. First, with impedance matching maximum value of the axial ratio occurs when C_λ = 0.85, for all values of κ. Second. For κ=0.02, axial ratio like return loss, records its highest value of close to 3dB, indicating that the antenna is then, just about circularly polarized. Third, for κ = 0.01 and 0.02, axial ratio values of the impedance-matched ENH are higher when C_λ is between 0.8 and 1.0, and smaller from that point up to when C_λ is about 1.1; thereafter, the axial ratio is about the same for both unmatched and impedance-matched antennas. When κ = 0.04 and 0.06, the axial ratio for the impedance-matched ENH is higher up to C_λ equals 1.1 and 1.3, respectively, after which its values become about the same as those for unmatched ENH. One other notable property of the axial ratio profiles is that the 3dB bandwidth remained the same at 54.55% for both the impedance-matched and unmatched ENHs, though for the case of κ = 0.02 (for which the best value of return loss was recorded), this is just about true. It might be possible in this case to adapt a recent theory reported in [23] to design an impedance matching network that significantly improves axial ratio performance.

Finally, the power gain curves of the ENH with and without impedance-matching circuitry are shown in Fig. 12.

The gain profiles indicate that for κ = 0.01 and 0.02, the differences in power gains for both ENH configurations are appreciable when C_λ is less than 1.1, however for C_λ greater than 1.1, both matched and unmatched ENHs, to a large extent, have approximately equal power gain. On the other hand, for higher values of κ, that is, 0.04 and 0.06, the power gain profiles are closer, except when C_λ is less than 1.0, for which the maximum differential in power of about 1.5dB is recorded. Indeed, the maximum power gain changed only slightly from 14.19dB for the unmatched ENH to 14.18dB for the impedance-matched antenna.

These observations concerning axial ratio and power gain are noteworthy because they suggest that impedance matching of the type utilized here does not lead to significantly noticeable deformations of the radiation-zone field patterns or deteriorations in the associated performance metrics of the ENH. It is important to remark, however, that the profiles of Fig.5 and 7 suggest that in general, improvements in return loss performance through impedance matching are at the expense of power gain.

4 Concluding Remarks

In addition to investigating the effects of impedance-matching circuitry on the input and radiation characteristics of an exponentially non-uniform helical antenna (ENH) mounted above a finite circular ground plane, this paper has also examined the influence of the degree of non-uniformity on the ENH's performance. Following a comprehensive formulation of the antenna's radiation field expressions via a vector magnetic potential approach, the distribution of current along the ENH's axis became available through a method of moments solution. Computational results obtained and

discussed in the paper demonstrate that the ENH's return loss is significantly enhanced by the incorporation of a single wire that extends over the quarter of the first turn of the ENH, as the impedance-matching network. The results also suggest that return loss for the impedance-matched ENH clearly depends on the degree of exponential non-uniformity specified by the parameter κ. According to the results, although axial ratio and power gain profiles naturally differ for the unmatched and impedance-matched ENH, the differences are not indicative of performance deterioration. Both the impedance-matched and unmatched ENHs have the same axial ratio bandwidth of 54.55%, and the maximum power gain of the unmatched ENH is only marginally greater than that of the matched ENH by 0.01 dB. It may be concluded, therefore, that the ENH can be impedance-matched to a 50Ω coaxial cable without loss of the advantages due to the antenna's geometrical non-uniformity. Nonetheless, the paper's computational results suggest that improvements in return loss are achieved at the expense of antenna gain. A future investigation involving the use of an optimization algorithm should establish optimum impedance-matched ENU parameters for specific applications.

References

[1] R. Stegen, "Impedance matching of helical antennas," in *IEEE Transactions on Antennas and Propagation*, vol. 12, no. 1, pp. 125-126, January 1964

[2] J. Kraus, "A 50-ohm input impedance for helical beam antennas," in *IEEE Transactions on Antennas and Propagation*, vol. 25, no. 6, pp. 913-913, November 1977.

[3] D. E. Baker, "Measured performance of a broadband matching section for peripherally fed helical antennas," in *Transactions of the South African Institute of Electrical Engineers*, vol. 76, No. 2, pp. 56-61, June 1985

[4] C. H. Chen, B. J. Hu, Z. H. Wu and E. K. N. Yung, "A Self-matching Hemispherical Helical Antenna," *IEEE Antennas and Propagation Society International Symposium.* pp. 4709-4712, *2006*.

[5] Shiqiang Fu, Yuan Cao, Yue Zhou, and Shaojun Fang, "Improved Low-Profile Helical Antenna Design for INMARSAT Applications", *International Journal of Antennas and Propagation* Volume 2012 | Article ID 829371 2012

[6] Slobodan V. Savić, Milan M. Ilić, and Antonije R. Djordjević, "Design of Internal Wire-Based Impedance Matching of Helical Antennas Using an Equivalent Thin-Wire Model", *International Journal of Antennas and Propagation* Volume 2017, Article ID 7365793, 5 pages. 2017

[7] S. V. Savić, M. M. Ilić and A. R. Djordjević, "Influence of Wire-Based Impedance-Matching on Helical Antenna Radiation," 2018 *26th Telecommunications Forum (TELFOR),* pp. 1-4, 2018.

[8] Hossein Mardani, Neil Buchanan, Robert Cahill, Vincent Fusco," Impedance Matching of Axial Mode Helical Antennas", *WSEAS TRANSACTIONS on CIRCUITS and SYSTEMS*, Volume 20, 2021, PP. 66-69, 2021.

[9] Chen, C., Yung, E.K., Hu, B., & Xie, S. (2007). Axial mode helix antenna with exponential spacing. *Microwave and Optical Technology Letters*, 49(7), pp. 1525-1530, July 2007

[10] G. Zhou, "A non-uniform pitch dual band helix antenna," *IEEE Antennas and Propagation Society International Symposium. Transmitting Waves of Progress to the Next Millennium. 2000 Digest*. Held in conjunction with: USNC/URSI National Radio Science Meeting (C, 2000), pp. 274-277 2000.

[11] H. M. Elkamchouchi and A. I. Salem, "Helical antennas with nonuniform helix diameter," *Proceedings of the Eighteenth National Radio Science Conference.* NRSC' (IEEE Cat. No.01EX462), 2001, pp. 143-152 2001.

[12] J. Dinkić, D. Olćan, A. Djordjević and A. Zajić, "Comparison of the Optimal Uniform and Nonuniform Lossy Helical Antennas," *2020 IEEE International Symposium on Antennas and Propagation and North American Radio Science Meeting*, 2020, pp. 423-424, 2020.

[13] A. A. Ayorinde, S. A. Adekola, and A. I. Mowete "Logarithmically-Wound Helix Antenna Excited for Axial-Mode Operations", *Jordan Journal of Electrical Engineering*, Volume 7, Number 3, September 2021. PP. 265-287. 2021

[14] Mowete, A. A. Ayorinde, and S. A. Adekola, "The Logarithmically-non-uniform Helix Antenna Mounted Above a Finite Ground Plane", *ELEKTRIKA Journal of Electrical Engineering*, VOL. 21, NO. 1, 2022, PP. 25-34. 2022

[15] S, A. Adekola, "On the excitation of a circular loop antenna by travelling- and standing-wave current distributions", *International Journal of Electronics*, 54, pp. 705-732, 1983.

[16] A. A. Ayorinde, S.A. Adekola, and A. Ike Mowete, "Analysis of a Circular-loop Antenna Backed by a Circular Ground-plane of Finite Extent", *Proceeding, Progress in Electromagnetics Research Symposium (PIERS)*, St. Petersburg, Russia. PP. 1-6, 2017.

[17] R. F. Harrington, "*Field computation by moment methods*," The Macmillan Book Company, New York, 1968.

[18] T. S. Bird, "Definition and Misuse of Return Loss [Report of the Transactions Editor-in-Chief]," in *IEEE Antennas and Propagation Magazine*, vol. 51, no. 2, pp. 166-167, April 2009.
[19] H. Nakano, and J. Yamauchi, "Characteristics of modified spiral and helical antennas," *IEE Proc. Microw. Ant. & Prop*., vol.129, No. 5, pp. 232-237. 1982.
[20] W. L. Stutzman, and G. A. Thiele, *Antenna theory and design*. John Wiley & Sons, New York, pp. 306-374. 1981.
[21] J. D. Kraus, "Helical beam antenna," *Electronics*, pp. 109- 111 April 1947,
[22] J. D. Kraus, "*Antennas*," McGraw-Hill, Inc., USA, 2nd Edition, pp.1-85, 265-339, 388-408: 1988,
[23] H. Nakano, T. Abe, A. Mehta and J. Yamauchi, "Theoretical Consideration of Axial Ratio Deterioration in CP Loop-Shaped Antennas," in *IEEE Antennas and Wireless Propagation Letters*, Vol. 22 No. 5., PP. 1035-1039, 2023.

Ayotunde Ayorinde received the degrees of B.SC, M.SC. and Ph.D. degrees in Electrical Engineering, from the University of Lagos, (UNILAG) Nigeria, in 1990, 1993, and 2009, respectively. His current research interests include electromagnetic fields, microwave engineering, antennas, and propagation. He belongs to the team that pioneered the Quasi-Moment Method (QMM) empirical modeling tool. Dr. Ayorinde is a Senior Lecturer at the University of Lagos and is also a member of the British Institution of Engineering and Technology (MIET) and a Registered Engineer in Nigeria.

Sulaiman Adeniyi Adekola was awarded the degree of B.Eng. (Hons.) Electrical Engineering at the Ahmadu Bello University (ABU) Zaria, Nigeria, 1968; M. Sc. Electrical Engineering at the Ohio State University, Columbus, Ohio, USA, 1972; Ph.D. in Engineering at the Ohio State University, Columbus, Ohio, USA, 1975. His research interests extend to Engineering Electromagnetics, Antenna Analysis & Design, Applied mathematics, Communications, empirical modeling with QMM (pioneer), and Digital Signal Processing. An Emeritus Professor, Electrical & Electronics Engineering, UNILAG, 2019; AAdekola is a Fellow, of the British Institution of Engineering & Technology (FIET), 1988; Fellow, of the Acoustical Society of America (FASA), 1988, Fellow, of the Nigerian Society of Engineers (FNSE), 1994; Fellow, Nigerian Academy of Science (FAS), 1990; Foundation Fellow, Nigerian Academic of Engineering (FAEng.), 1999; Life Snr Member, IEEE, USA, 2011; and a Chartered Engineer (C. Eng.).

Ike Mowete obtained the degrees of B.Sc. (1980), M. Sc. (1983), and Ph.D. (1990) all in electrical engineering from the University of Lagos, Akoka, Lagos, in Nigeria. His Ph.D. thesis was on a "quasi-static moment-method analysis of microstrip antennas". He has published quite a few papers on microstrip antennas, dielectric-costed thin-wire antennas, shielding effectiveness of planar shields, and pioneering contributions concerning QMM-based empirical models for path-loss prediction, energy demand forecasting, and rain attenuation prediction. His current research interests include thin-wire antenna structures, applications of the theory of characteristic modes to antenna analysis and design, and spectrum engineering issues. Professor Mowete, who teaches numerical methods, circuit theory, and antennas and propagation at the University of Lagos is a member of the IEEE.